

**Magnetotransport in Fe-intercalated  $TS_2$ : Comparison between  $T = \text{Ti}$  and  $\text{Ta}$** Jesse Choe,<sup>1</sup> Kyungmin Lee,<sup>2</sup> C.-L. Huang,<sup>3</sup> Nandini Trivedi,<sup>2</sup> and E. Morosan<sup>1,3,\*</sup><sup>1</sup>*Department of Electrical and Computer Engineering, Rice University, Houston, Texas 77005, USA*<sup>2</sup>*Department of Physics, The Ohio State University, Columbus, Ohio 43210, USA*<sup>3</sup>*Department of Physics and Astronomy, Rice University, Houston, Texas 77005, USA*

(Received 2 November 2018; published 19 February 2019)

Sharp magnetization switching and large magnetoresistance (MR) were previously discovered in single crystals of  $2\text{H-Fe}_x\text{TaS}_2$  and attributed to the Fe superstructure and its defects. We report similar sharp switching and large MR in  $1\text{T-Fe}_x\text{TiS}_2$  ( $0.086 \leq x \leq 0.703$ ) while providing a side-by-side comparison of the only two such ferromagnetic transition-metal dichalcogenides. The switching field  $H_s$  and MR values are similar in both  $1\text{T-Fe}_x\text{TiS}_2$  and  $2\text{H-Fe}_x\text{TaS}_2$ , with a larger than expected bowtie  $\rho(H)$  and a sharper hysteresis loop for  $H \parallel c$  in the former. The Curie and Weiss temperatures remain roughly constant below  $x \sim 1/3$  in the  $T = \text{Ti}$  single crystals before increasing monotonically for higher  $x$ , while  $H_s$  and MR reach maxima where defects in the superstructure exist, or a minimum near superstructure compositions, and they remain constant above  $x \sim 0.4$ . Despite previous reports, electron diffraction shows only the  $\sqrt{3} \times \sqrt{3}$  superstructure in  $1\text{T-Fe}_x\text{TiS}_2$ . Glassy behavior is shown to coexist within the ferromagnetic state in  $1\text{T-Fe}_x\text{TiS}_2$  for compositions between 0.1 and 0.703. A simple theoretical model considering first-, second- and third-neighbor interactions yields a phase diagram that accounts for both spin glass behavior and different superstructures.

DOI: [10.1103/PhysRevB.99.064420](https://doi.org/10.1103/PhysRevB.99.064420)**I. INTRODUCTION**

Transition-metal dichalcogenides (TMDCs) have garnered interest due to their potential use in a variety of applications. While materials like  $\text{MoS}_2$  have long been used as mechanical lubricants [1], recent interest has focused on the magnetic and electrical properties of layered TMDCs. Due to the two-dimensional nature of these materials, many display charge-density waves and superconductivity, competing electronic states driven by Fermi surface instabilities [2–8]. The choice of transition metal *and* polytype drastically affects the electrical properties in the layered TMDCs, such that insulators ( $\text{HfS}_2$  [9]), semiconductors ( $\text{MoS}_2$  [10],  $\text{WS}_2$  [11]), semimetals ( $\text{WTe}_2$  [12],  $\text{TcS}_2$  [13]), and metals ( $\text{NbS}_2$  [14],  $\text{VSe}_2$  [15]) with or without superconductivity ( $\text{NbSe}_2$  [4],  $2\text{H-TaS}_2$  [6]) can all be found within the TMDC archetype.

Chemical modifications through intercalation or doping impart a new level of complexity in both the electronic and magnetic properties of TMDCs. For electronic properties, copper or palladium intercalation induces superconductivity in  $1\text{T-TiSe}_2$  [3,5], while doping Pt on the Ti site leads to insulating behavior [16]. Similarly, intercalating small amounts of Cu in  $2\text{H-TaS}_2$  increases the superconducting temperature [7]. Regarding magnetism, unusual properties like very large, nonsaturating magnetoresistance (MR) can be seen in undoped  $\text{WTe}_2$  [12], while magnetic intercalation often induces antiferromagnetic order [17]. These results all raise questions about the role of the intercalant in different TMDCs and different polytypes.

When surveying the magnetically intercalated TMDCs, two materials stand out for their magnetotransport properties not seen in other TMDCs:  $2\text{H-Fe}_x\text{TaS}_2$  and  $1\text{T-Fe}_x\text{TiS}_2$  order ferromagnetically with the moments parallel to the  $c$  axis. They also both display large (up to 150%) MR, while normal metals only show MR values up to a few percent. This prompts the need for an in-depth comparison between the two compounds, as well as a comparison with other intercalated TMDCs, to address a few outstanding questions: (i) Why do these two systems show FM order along the  $c$  axis while most other magnetically intercalated TMDCs order antiferromagnetically or ferromagnetically along the  $ab$  plane [18–23]? (ii) Given the substantive differences between Ti and Ta [number of  $d$  electrons, atomic size,  $TS_6$  coordination polyhedra (Fig. 1)], what singles out these two compounds from other similar TMDCs intercalated with Fe as ferromagnets, with large MR? (iii) Why is there a progression from the  $2 \times 2$  superstructure to the  $\sqrt{3} \times \sqrt{3}$  in  $2\text{H-Fe}_x\text{TaS}_2$ , while  $1\text{T-Fe}_x\text{TiS}_2$ , as is shown below, remains in the  $\sqrt{3} \times \sqrt{3}$  superstructure for the whole Fe composition range? (iv) Why does glassy behavior appear in  $1\text{T-Fe}_x\text{TiS}_2$ , as our present measurements reveal, and antiferromagnetic behavior appear in  $2\text{H-Fe}_x\text{TaS}_2$  for certain  $x$  regimes?

In the hexagonal  $2\text{H-TaS}_2$  system, Fe intercalation results in ferromagnetic (FM) order for  $x \leq 0.4$  and antiferromagnetic (AFM) order above  $x > 0.4$  [24]. In the FM state,  $2\text{H-Fe}_x\text{TaS}_2$  shows high magnetic anisotropy and an easy axis parallel to  $c$ . The Fe atoms form  $2 \times 2$  and  $\sqrt{3} \times \sqrt{3}$  superstructures at  $x = 1/4$  and  $1/3$ , respectively. For  $x = 1/4$ , the magnetization shows sharp switching, resulting in rectangular isothermal magnetization curves [25]. Fe concentrations away from  $x = 1/4$  reveal an increase in MR, from  $< 1\%$  at the

\*emorosan@rice.edu

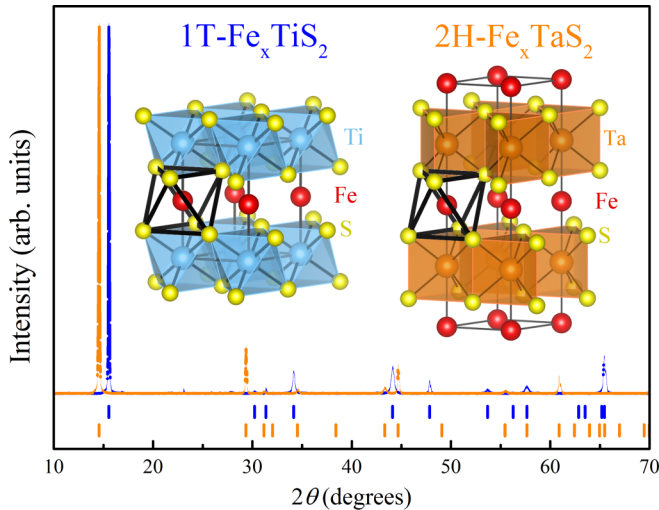


FIG. 1. X rays and ticks for  $\text{Fe}_x\text{TiS}_2$  and  $\text{Fe}_x\text{TaS}_2$ . Insets: crystal structure for  $\text{Fe}_x\text{TiS}_2$  (left) and  $\text{Fe}_x\text{TaS}_2$  (right). Note the octahedral coordination for the Fe atoms in both structures.

$x = 1/4$  superstructure to  $\sim 140\%$  at  $x = 0.29$ , attributed to spin disorder scattering [26,27].

Much less is known about  $1\text{T-Fe}_x\text{TiS}_2$ . However, the previously known properties, together with our findings, point to four substantive differences between the two  $\text{Fe}_x\text{TS}_2$  ( $T = \text{Ti}$  and  $\text{Ta}$ ) systems. First, there are key structural differences due to the different polytypes as illustrated in Fig. 1. In the  $2\text{H}$  polytype of  $\text{TS}_2$ , the S atoms form a trigonal-prismatic coordination around  $T$  (Fig. 1, left inset), and the unit cell consists of two  $\text{TS}_2$  layers in an  $ABAB\dots$  stacking along  $c$  (with a  $60^\circ$  rotation between the  $A$  and  $B$  planes).  $\text{TiS}_2$  is only known to exist in the  $1\text{T}$  polytype, with one  $\text{TS}_2$  layer per unit cell (and an  $AAA\dots$  layer stacking) and octahedral  $T$  coordination (Fig. 1, right inset). It is important to note that, despite the different polytypes, the Fe atoms are octahedrally coordinated for both (black lines in the insets). The second difference is the electron count:  $\text{Ti}^{4+}$  is in a  $3d^0$  electronic configuration, whereas  $\text{Ta}^{4+}$  is in the  $5d^1$  configuration, which can be expected to result in differences in the electrical transport, even for the pure  $\text{TS}_2$ . The third key difference is revealed in the properties of these two materials upon Fe intercalation: glassy behavior exists in  $1\text{T-Fe}_x\text{TiS}_2$  [18,28–30] but not in  $2\text{H-Fe}_x\text{TaS}_2$  [25]. Here we will show ac susceptibility data for  $1\text{T-Fe}_x\text{TiS}_2$ , suggesting the *coexistence* of the glassy state within the ferromagnetic order for  $x = 0.086\text{--}0.7$ , rather than a progression with  $x$  from glassy to FM as previously reported [31]. The final difference is that in  $1\text{T-Fe}_x\text{TiS}_2$ , our electron diffraction measurements indicate a  $\sqrt{3}\times\sqrt{3}$  superstructure down to the lowest composition measured,  $x = 0.086$ , with no  $2\times 2$  superstructure, as was the case in  $2\text{H-Fe}_x\text{TaS}_2$  near  $x = 1/4$  [25].

Motivated by the similarities with the better studied  $2\text{H-Fe}_x\text{TaS}_2$ , in the present paper we turn to the less studied  $1\text{T-Fe}_x\text{TiS}_2$  ( $x = 0.086\text{--}0.703$ ) system, the only other known TMDC with FM moment ordered along the  $c$  axis and sharp magnetization switching. Following a detailed characterization of the properties of  $1\text{T-Fe}_x\text{TiS}_2$  single crystals, we will focus on a comparison between the Fe-intercalated Ti and

Ta disulfide systems, as well as contrasting these two Fe-intercalated ferromagnets to the other magnetically intercalated TMDCs.

## II. METHODS

Single crystals of  $1\text{T-Fe}_x\text{TiS}_2$  were grown using iodine vapor transport. Stoichiometric amounts of Fe, Ti, and S powders were sealed in evacuated quartz tubes ( $\approx 6$  in. in length, 0.5 in. in diameter) with approximately 50%  $\text{I}_2$  by mass. The tubes were then placed in a gradient furnace. The samples were heated for at least 10 days at a gradient of  $900\text{--}800^\circ\text{C}$ , then cooled to room temperature. Iron compositions  $x = 0.086\text{--}0.703$  were determined by inductively coupled plasma atomic emission spectroscopy measurements performed by Galbraith Laboratories.

Powder x-ray diffraction was performed using a Bruker D8 Advance diffractometer, and refinements were performed using the EVA/TOPAS software suite. The x-ray data shown in Fig. 1 confirm the  $1\text{T}$  polytype for all Ti samples in this study, in contrast to the  $2\text{H}$  polytype of the Fe-intercalated  $\text{TaS}_2$  [25]. Magnetization measurements were performed using a Quantum Design (QD) Magnetic Property Measurement System (MPMS). Transport measurements were performed using a QD Physical Property Measurement System (PPMS), using standard four-point probe measurements with  $i\parallel ab$  and  $H\perp ab$ . The ac susceptibility was measured using the ac magnetic susceptibility (ACMS) insert in the QD PPMS. All measurements were performed on bulk crystals tens of microns in thickness.

Electron microscopy was performed on a JEOL 2100F operated at 200 kV. Electron diffraction was performed with an effective camera length of 50 cm and collected on an ES500W camera from Gatan, Inc. Samples for transmission electron microscopy (TEM) were prepared by shearing large crystals submerged in acetone in a mortar and pestle. The powdered material was isolated and drop cast onto a carbon grid with a copper frame and allowed to dry under a stream of dry nitrogen before use.

## III. RESULTS

As previous measurements indicated [32],  $1\text{T-Fe}_x\text{TiS}_2$  is a ferromagnet with the moments perpendicular to the TMDC layers. Figure 2(a) illustrates the anisotropic magnetic susceptibility  $M/H$  near  $T_C$  for  $x = 0.197$ , while Fig. 2(b) demonstrates Curie-Weiss behavior at high temperatures. We find that  $T_C$  ranges from 35 K all the way up to 140 K for  $x = 0.087\text{--}0.703$ , and the ordering temperatures are fairly close to the Weiss temperatures  $\theta_W$ , determined from linear fits as shown in Fig. 2(b) (solid line).

While magnetic order and the anisotropy in  $1\text{T-Fe}_x\text{TiS}_2$  are similar to those in  $2\text{H-Fe}_x\text{TaS}_2$ , TEM data for  $1\text{T-Fe}_x\text{TiS}_2$  show *only* the  $\sqrt{3}\times\sqrt{3}$  superstructure for the whole  $x$  range in the current study (see Table I). No  $2\times 2$  superstructure close to the  $x = 1/4$  (or any other composition) in contrast to the Ta analog [25]. The  $\sqrt{3}\times\sqrt{3}$  superstructure for  $1\text{T-Fe}_{0.197}\text{TiS}_2$  is seen in the TEM image in Fig. 2(c). The blue outline (inner diamond) corresponds to the  $1\text{T-TiS}_2$  structure, while the orange (outer diamond) depicts the  $\sqrt{3}\times\sqrt{3}$  superstructure upon Fe intercalation. It would appear that the polytype, the size of

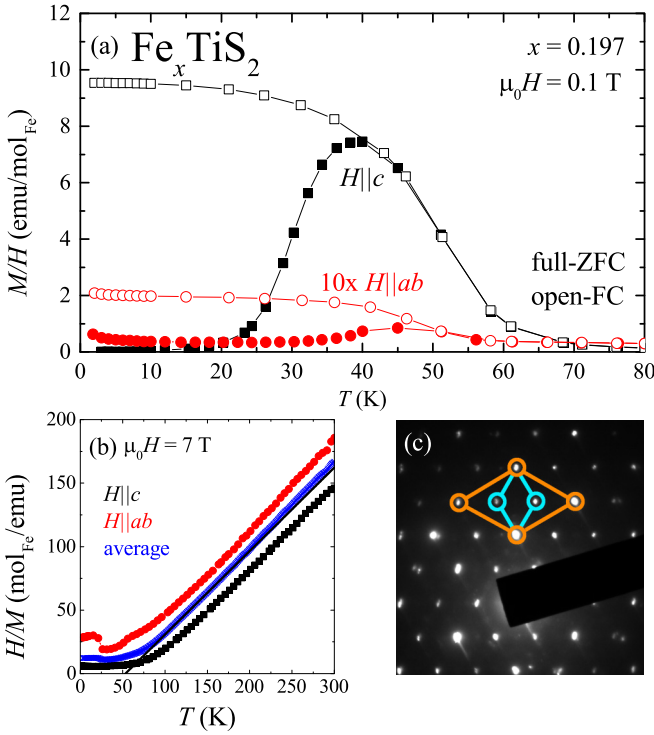


FIG. 2. (a) ZFC (open) and FC (closed) temperature-dependent magnetic susceptibility for both  $H \parallel c$  (square) and  $H \parallel ab$  (circle) for  $\text{Fe}_{0.197}\text{TiS}_2$  at  $\mu_0 H = 0.1$  T. (b) Inverse susceptibility fit at  $\mu_0 H = 7$  T. The black line shows a Curie-Weiss fit of the averaged data. (c) Electron diffraction pattern for  $\text{Fe}_{0.197}\text{TiS}_2$  showing the  $\sqrt{3} \times \sqrt{3}$  superstructure.

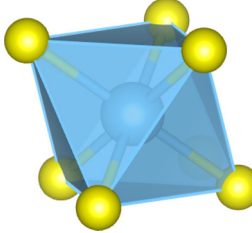
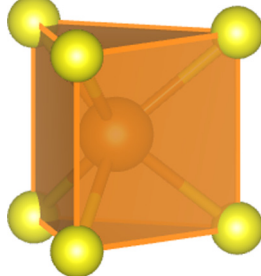
the transition metal  $T$ , the amount of intercalant, and the potential geometric frustration all contribute to the exchange interactions. Our model calculation, presented below, suggests that the superstructures are a result of the relative strengths of the exchange interactions. This also ties in with another

significant difference between the two series, which will be discussed later: the Ti compounds exhibit reentrant spin glass behavior in the ferromagnetic state, whereas the Ta analogs do not.

Despite the differences between the two series, Fig. 3 highlights the similar features of  $1\text{T-Fe}_x\text{TiS}_2$  to those of  $2\text{H-Fe}_x\text{TaS}_2$ , which set both compounds apart from other intercalated TMDCs. Anisotropic magnetization isotherms show drastic variation with composition for  $1\text{T-Fe}_x\text{TiS}_2$  (full symbols, Fig. 3), similar to the  $M(H)$  behavior in  $2\text{H-Fe}_x\text{TaS}_2$  (Fig. 4 in Chen *et al.* [27]). Sharp hysteresis loops were first observed in  $2\text{H-Fe}_{1/4}\text{TaS}_2$  [25]. As a function of  $x$ , the switching field  $H_s$  decreased for  $0.25 < x < 0.35$  [27]. The similarities between the sharp hysteresis loops in both  $T = \text{Ta}$  and  $\text{Ti}$  series motivated MR measurements on  $1\text{T-Fe}_x\text{TiS}_2$ , since very large MR values (up to  $\sim 140\%$ ) were discovered in  $2\text{H-Fe}_x\text{TaS}_2$  [26]. Indeed, MR curves (open symbols, Fig. 3) are remarkably similar to those in  $2\text{H-Fe}_x\text{TaS}_2$  [25,27]. The “bowtie” curves display a sharp resistivity drop at the same  $H_s$  field as the sharp magnetization switch for  $H \parallel c$  (black symbols, Fig. 3). MR values vary with  $x$  ranging from a few percent to 41% at  $x = 0.197$ . While smaller than most MR values in  $2\text{H-Fe}_x\text{TaS}_2$  [27], the  $1\text{T-Fe}_x\text{TiS}_2$  MR reaches values larger than the few percent typically seen in normal metals, and larger than previously reported [28].

Existing measurements on  $\text{Fe}_x\text{TiS}_2$  reported spin glass ( $0 < x < 0.2$ ) behavior, cluster glass ( $0.2 < x < 0.4$ ) behavior [33], and long-range ferromagnetic order ( $0.4 < x < 1.0$ ) [34,35]. With ac magnetic susceptibility measurements on  $1\text{T-Fe}_x\text{TiS}_2$ , we confirm glassy behavior for  $x = 0.1-0.703$  (see Appendix B) with important differences from the previously reported magnetic properties across the series. Previous studies on polycrystalline  $\text{Fe}_x\text{TiS}_2$  show glassy behavior at low intercalant concentrations ( $x < 0.4$ ), and ferromagnetic order for  $0.4 < x < 1.0$  [34,35]. Our measurements on single crystals suggest cluster glass behavior for concentrations  $0.1 \leq x \leq 0.7$  (Appendix B). Our single-crystal measurements

TABLE I. Comparison between the  $1\text{T-Fe}_x\text{TiS}_2$  and  $2\text{H-Fe}_x\text{TaS}_2$  systems.  $\mu$  denotes magnetic moment.

	$1\text{T-Fe}_x\text{TiS}_2$	$2\text{H-Fe}_x\text{TaS}_2$
Stacking		
$T$ coordination	$A-B-C$ Octahedral	$A-B-A$ Trigonal prism
Magnetic ordering	$0.09 \leq x \leq 0.7$	$x < 0.4$ $x > 0.4$
Known superstructure	FM ( $\mu \parallel c$ ) + glassy behavior $0.09 \leq x \leq 0.7$ $\sqrt{3} \times \sqrt{3}$	FM ( $\mu \parallel c$ ) AFM $x = 0.25$ $0.264 < x < 0.33$ $2 \times 2$ $\sqrt{3} \times \sqrt{3}$
Sharp magnetization switching	$0.197 < x < 0.7$	$0.246 < x < 0.348$
MR	$\sim 0.3\%$ to $\sim 41\%$	$\lesssim 1\%$ to $\sim 140\%$

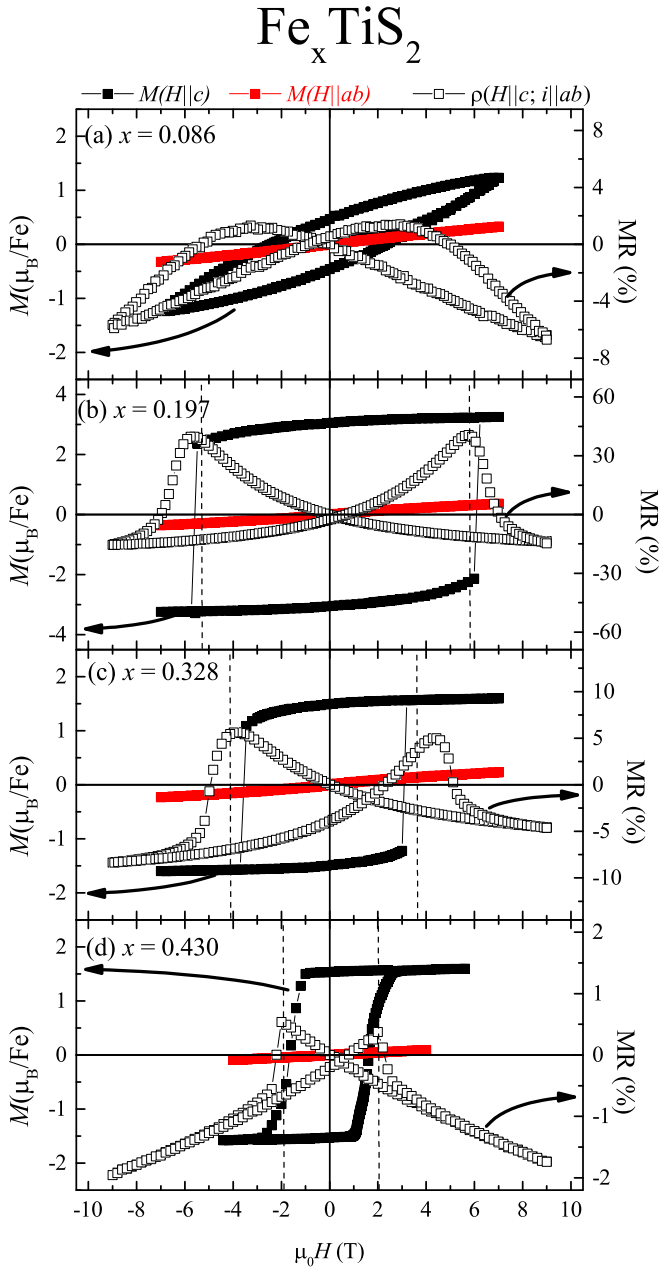


FIG. 3. Magnetization for  $H \parallel c$  (closed, square),  $H \parallel ab$  (closed, circle), and magnetoresistance  $MR = \frac{\rho(H) - \rho(0)}{\rho(0)}$  for  $H \parallel c$ ,  $i \parallel ab$  (open, circle) at  $T = 2$  K.

resolve this apparent inconsistency by showing *coexistence* of cluster glass behavior within the ferromagnetic order for  $x = 0.1-0.703$  and  $H \parallel c$ , but not for  $H \parallel ab$  (Fig. 4). Additionally, frequency dependent ac susceptibility measurements were previously only taken for low concentrations ( $x < 0.33$ ), so glassy behavior at higher concentrations had not been tested [29]. Our ac susceptibility measurements at different dc fields show that the peak in susceptibility splits into two distinct peaks with increasing field. For example, for  $x = 0.2$  [Fig. 4(a)], the splitting occurs around  $\mu_0H = 0.3$  T, with the freezing temperature  $T_f$  (blue diamonds) moving down with increasing field as expected for glassy behavior. Conversely, the ferromagnetic order occurs at increasingly higher  $T_C$  (red

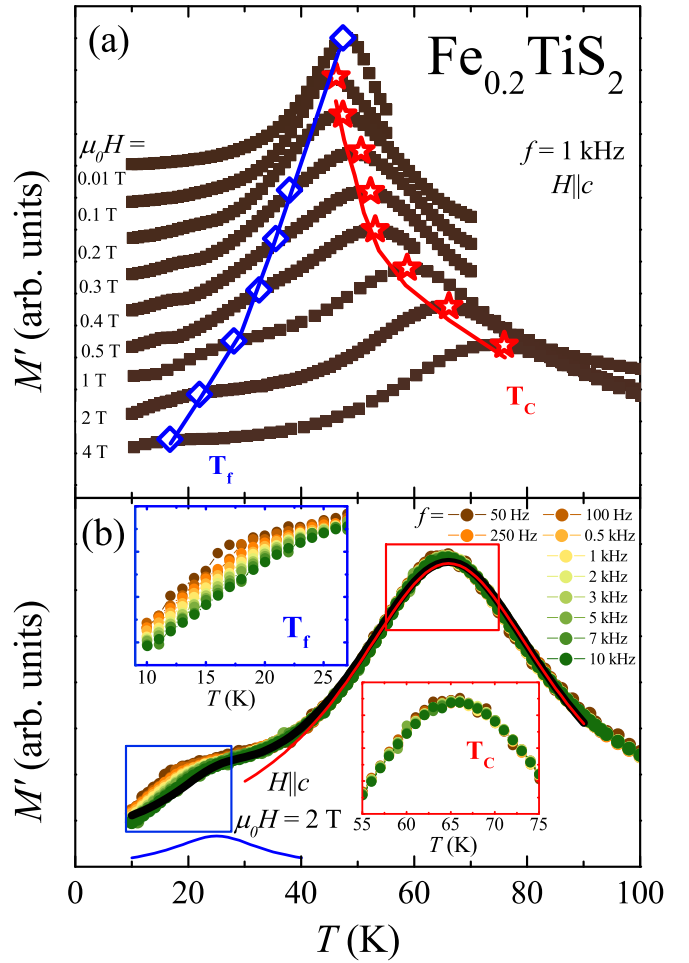


FIG. 4. (a) Field-dependent susceptibility showing splitting of freezing temperature  $T_f$  (diamonds) and Curie temperature  $T_C$  (stars) with increasing field. Curved lines are a guide to the eye. (b) Frequency-dependent susceptibility showing frequency splitting around the low temperature  $T_f$  and no frequency splitting around  $T_C$ . Curves show low peak (blue), high peak (red), and combined (black) fits for the peaks.

stars) as  $H$  increases. Figure 4(b) shows the  $\mu_0H = 2$  T ac susceptibility for  $x = 0.2$ , with clear frequency dependence for the low-temperature peak, and no frequency dependence at  $T_C$ . The solid lines are fits for the two peaks illustrating how the  $T_f$  and  $T_C$  values were determined from the  $M'(T)$ .

#### IV. DISCUSSION

Sharp magnetization switching in TMDCs was first observed in  $2H\text{-Fe}_x\text{TaS}_2$  [25]. While intriguing by itself, this behavior also appears correlated with large MR in  $2H\text{-Fe}_x\text{TaS}_2$  single crystals [26]. Similar magnetization isotherms were reported in  $1T\text{-Fe}_x\text{TiS}_2$  [32], and the existence of large MR is shown in Fig. 3. Large MR effects in homogeneous metals are of fundamental interest, as well as for potential applications in magnetic sensing. This motivated our comparative study of the only two magnetically intercalated TMDCs known to exhibit such unusual magnetotransport properties. Our aim

was answering why, unlike any other magnetic  $3d$  metals, Fe intercalation results in axial ferromagnetic order with sharp  $M(H)$  isotherms and large MR, and why this behavior appears in Fe intercalated  $1\text{T-TiS}_2$  and  $2\text{H-TaS}_2$  and not other Fe intercalated TMDCs, which tend to order antiferromagnetically along  $c$ . In the course of the current investigation on  $1\text{T-Fe}_x\text{TiS}_2$ , we also revealed additional questions regarding the Fe superstructures by contrast to that in  $2\text{H-Fe}_x\text{TaS}_2$ , as well as the coexistence of glassy behavior within the ferromagnetically ordered state. The similarities and differences between  $1\text{T-Fe}_x\text{TiS}_2$  and  $2\text{H-Fe}_x\text{TaS}_2$  are summarized below, together with a theoretical discussion offering insight into the magnetic properties of these two systems.

Understanding  $1\text{T-Fe}_x\text{TiS}_2$  requires that it be placed in context with  $2\text{H-Fe}_x\text{TaS}_2$  and other magnetically-intercalated TMDCs. One of the key differences of Fe intercalation, compared to other magnetic  $3d$  metals, is the easy axis anisotropy. Intercalation of Fe atoms into a TMDC structure tend to result in the moment ordering along the  $c$  axis. In both  $1\text{T-Fe}_x\text{TiS}_2$  and  $2\text{H-Fe}_x\text{TaS}_2$  where FM ordering occurs, the Fe atoms are located between the layers surrounded by S ions forming distorted octahedra [Figs. 1(a) and 1(b)] (with local point group  $D_{3d}$ ). Crystal field theory predicts that, in the intercalated Fe ions, the orbitals with out-of-plane angular momenta form the lowest-energy manifold due to the  $c$ -axis elongation ( $e_g^\sigma$  orbitals, derived from  $t_{2g}$  orbitals without the distortion), leading to the strong magnetic anisotropy with easy axis along the  $c$ -axis [20,36]. A more recent theoretical study on  $2\text{H-Fe}_{1/4}\text{TaS}_2$  also found that the Fe ions have large, unquenched, out-of-plane orbital magnetic moments ( $\sim 1.0\mu_B$ ) [37]. On the other hand, for compounds with other intercalants such as Mn, Cr, or V, the outermost  $d$  shell is half- or less than half-filled. In the high spin configuration, due to Hund's coupling, the extra holes populate the  $e_g^\sigma$  orbitals with no out-of-plane angular momentum component [36], which is consistent with the easy-plane magnetic anisotropy of these compounds.

With regard to the superstructure for  $2\text{H-Fe}_x\text{TaS}_2$ , a  $2\times 2$  superstructure near  $x = 1/4$  [25] and a  $\sqrt{3}\times\sqrt{3}$  superstructure near  $x = 1/3$  are reported [25–27]. However, Choi *et al.* performed TEM on  $\text{Fe}_{1/4}\text{TaS}_2$ , which suggested the two superstructures exist in different domains of the same crystal [38]. Additionally, between  $x = 1/4$  and  $1/3$ , the superstructure is reported as the  $\sqrt{3}\times\sqrt{3}$  with vacancies [26]. For  $1\text{T-Fe}_x\text{TiS}_2$ , the same superstructures ( $2\times 2$  superstructure near  $x = 1/4$ , and a  $\sqrt{3}\times\sqrt{3}$  superstructure near  $x = 1/3$ ) were reported [39]; however, neutron results claim the  $\sqrt{3}\times\sqrt{3}$  for  $x = 1/3$  and  $2\sqrt{3}\times 2$  for  $x = 1/4$  [40–42]. In contrast, our electron-diffraction measurements on  $1\text{T-Fe}_x\text{TiS}_2$  show only the  $\sqrt{3}\times\sqrt{3}$  superstructure for  $0.196 \lesssim x \lesssim 0.374$ . For neutron diffraction, the data set is taken over a large area of sample while TEM and the electron diffraction are done on local areas. The  $2\sqrt{3}\times 2$  superstructure seen in neutron diffraction could be the result of a blending of the two superstructures. Alternatively, the calculated phase diagram in Figs. 6(e) and 6(f) show a phase space of potential superstructures, as a function of coupling strengths, that contains a superstructure with Bragg peaks at  $K$  and  $M$  consistent with a mixture of  $2\times 2$  and  $\sqrt{3}\times\sqrt{3}$  next to the  $\sqrt{3}\times\sqrt{3}$ . A small change in exchange energies could push the system from one superstructure to the other.

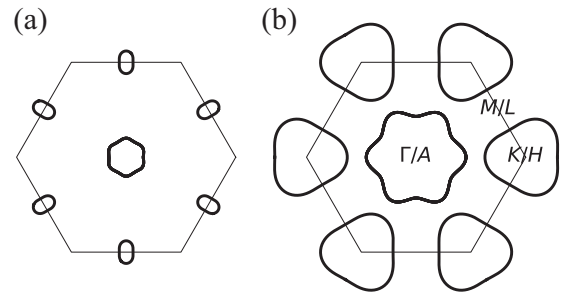


FIG. 5. Schematic Fermi surfaces of (a)  $1\text{T-TiS}_2$  and (b)  $2\text{H-TaS}_2$ , projected to the  $ab$  plane.  $1\text{T-TiS}_2$  band structure contains small Fermi pockets enclosing  $\Gamma/A$  and  $M/L$  points.  $2\text{H-TaS}_2$ , on the other hand, has large Fermi pockets enclosing  $\Gamma/A$  and  $K/H$  points.

Both  $1\text{T-Fe}_x\text{TiS}_2$  and  $2\text{H-Fe}_x\text{TaS}_2$  provide equivalent local environments (distorted octahedra) to the intercalated Fe ions. The difference—in superstructures and the glassy behavior—between the two families may therefore be attributed to the inter-Fe interactions. As suggested by the metallic transport behavior of these compounds, the interaction between the local moments of Fe is expected to be of Ruderman-Kittel-Kasuya-Yosida (RKKY) type [43–45], which is controlled by the underlying electronic structure of the charge carriers.  $2\text{H-TaS}_2$ , with  $\text{Ta}^{4+}$  in  $d^1$  configuration, has large Fermi pockets enclosing the  $\Gamma$  and  $K$  points [8] [Fig. 5(b)], resulting in short wavelength RKKY oscillations in  $2\text{H-Fe}_x\text{TaS}_2$ . It is estimated to be similar to the distance between nearest neighboring Ta ions [37]. The interaction between two Fe moments located at nearest-neighboring sites is thus antiferromagnetic, consistent with the negative Curie-Weiss temperature for larger doping in  $2\text{H-Fe}_x\text{TaS}_2$  [24]. On the other hand,  $1\text{T-TiS}_2$  contains  $\text{Ti}^{4+}$  in a  $d^0$  configuration, with small Fermi pockets enclosing  $\Gamma$  and  $L$  points [46] [Fig. 5(a)]. This leads to RKKY interaction in  $1\text{T-Fe}_x\text{TiS}_2$  with a spatial structure very different to that of the Ta counterpart. This, in turn, may be responsible for the lack of a  $2\times 2$  superstructure in  $1\text{T-Fe}_x\text{TiS}_2$ , and its glassy behavior may also be due to this difference in the Fe-Fe interactions.

## V. THEORETICAL MODELING

Here we present a model calculation demonstrating how the interaction between different ions can lead to different superstructures. Starting with a triangular lattice of size  $6\times 6$  that represents the available sites for the intercalated Fe ions, we choose a fraction of the sites  $\{\mathbf{r}_i\}$  to be Ising spins  $\{s_i = \pm 1\}$  for  $i = 1, \dots, 9$ , which model the Fe moments at a doping level of  $x = 1/4$ . To account for the different inter-Fe RKKY interactions, we adopt a model with nearest-, second-nearest-, and third-nearest-neighbor interactions, whose interaction energy is given by

$$E[\{\mathbf{r}_i, s_i\}] = J_1 \sum_{\langle \mathbf{r}_i, \mathbf{r}_j \rangle} s_i s_j + J_2 \sum_{\langle \mathbf{r}_i, \mathbf{r}_j \rangle_2} s_i s_j + J_3 \sum_{\langle \mathbf{r}_i, \mathbf{r}_j \rangle_3} s_i s_j. \quad (1)$$

We determine the optimal configuration  $\{\mathbf{r}_i, s_i\}_{i=1, \dots, 9}$  that minimizes this energy. Here  $\langle \cdot, \cdot \rangle$ ,  $\langle \cdot, \cdot \rangle_2$ , and  $\langle \cdot, \cdot \rangle_3$ , respectively, represent nearest-, second-nearest-, and third-nearest-neighboring sites, with Ising exchange constants  $J_1$ ,  $J_2$ , and  $J_3$ . We search for the optimal configuration at different values

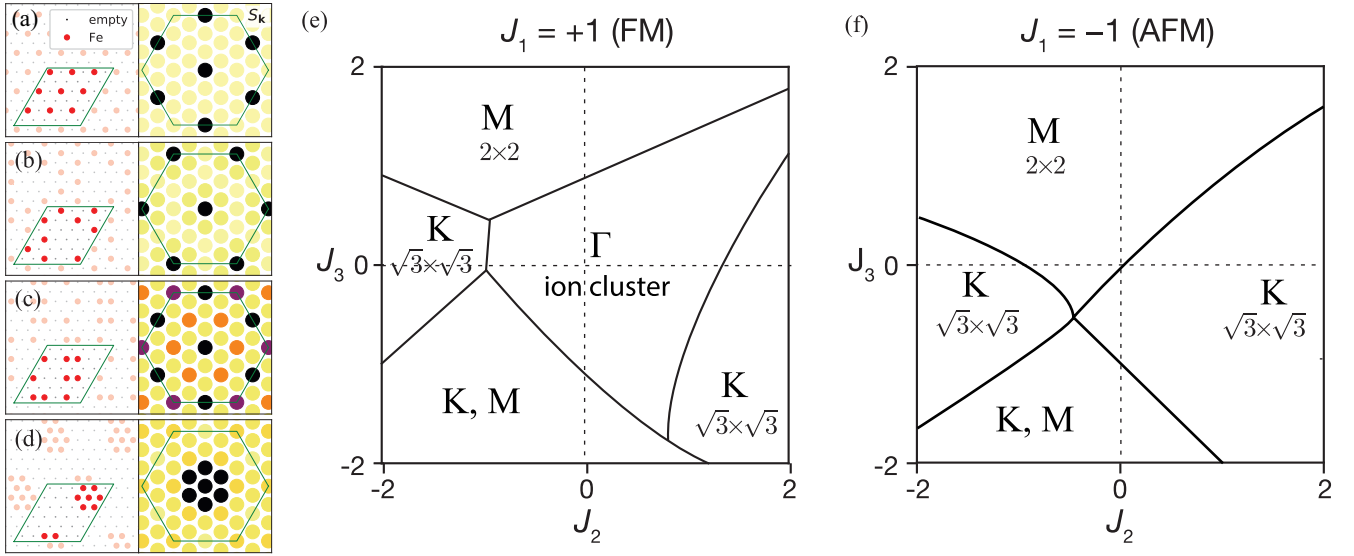


FIG. 6. (a)–(d) Locations of the intercalated ion (left panels) and corresponding structure factors (right panels) for (a) the  $2 \times 2$  superstructure, (b) the  $\sqrt{3} \times \sqrt{3}$  superstructure, (c) the “ $2 \times 2 + \sqrt{3} \times \sqrt{3}$ ” superstructure, and (d) the ion cluster phase. Note that for (b) and (c) the ions do not form perfect superstructures due to the presence of vacancies. The green lines mark the  $6 \times 6$  supercell used in the calculation and the Brillouin zone boundary. The structure factors have been symmetrized by the point-group symmetry of the undoped system. (e), (f) Phase diagram of the model in Eq. (1) at (e) ferromagnetic  $J_1 = 1$  and (f) antiferromagnetic  $J_1 = -1$ . The phases are labeled by the peak positions of structure factor  $S_{\mathbf{k}}$ .

of ( $J_1, J_2, J_3$ ) using simulated annealing to construct a phase diagram.

As a function of coupling constants, we find various superstructures, as illustrated in Figs. 6(a)–6(d). Figures 6(e) and 6(f) show the phase diagrams of this model for FM ( $J_1 = 1$ ) and AFM nearest-neighbor Ising exchange ( $J_1 = -1$ ), respectively. The phases are classified according to the peak position of the structure factor  $S_{\mathbf{k}} = |\sum_j e^{i\mathbf{k} \cdot \mathbf{r}_j}|$  and include the  $2 \times 2$  superstructure [ $S_{\mathbf{k}}$  peaked at  $M$ , panel (a)], the  $\sqrt{3} \times \sqrt{3}$  superstructure [peaked at  $K$ , panel (b)], a “ $2 \times 2 + \sqrt{3} \times \sqrt{3}$ ” superstructure [peaked at  $K$  and  $M$ , panel (c)], and an ion cluster phase [peaked at  $\Gamma$ , panel (d)].

It is important to point out that this simple model is constructed to demonstrate possible mechanisms of superstructure formation, and therefore is not expected to be quantitatively accurate. The small system size of  $6 \times 6$  and the limited number of interactions allows only a small number of structures. More importantly, the model calculation only searches for the equilibrium ground state. Experimentally, the structure of the intercalated ions is determined by quench dynamics, which depend on many factors, including relaxation time scales and finite-temperature entropic effects that are ignored in the present calculation.

Nevertheless, this model captures some key elements of the experimental system. FM interactions between nearest, second-nearest, and third-nearest neighbors promote superstructures with their corresponding length scales. In the presence of AFM interactions, competition between different interactions as well as geometrical frustration determine the structure.

One clear difference between the phase diagrams with AFM and FM  $J_1$  is the existence of the ion cluster phase for the latter. This occurs because with FM  $J_1$  interactions,

it is energetically favorable for the ions to form clusters. On the other hand with AFM  $J_1$ , the geometric frustration of the triangular lattice suppresses such clustering tendencies. The formation of ion clusters through such a mechanism could possibly explain the observed cluster glass behavior in the Ti compound, and the lack thereof in the Ta compound.

## VI. CONCLUSIONS

A summary of the magnetotransport parameters for  $1T\text{-Fe}_x\text{TiS}_2$  is provided in Figs. 7(a)–7(c) (a table of the values is provided in Appendix A).  $T_C$  [circles, left, Fig. 7(a)] and  $\theta_W$  [triangles, right, Fig. 7(a)] vary little with  $x$  below  $x \approx 0.4$ , while  $H_s$  [squares, right, Fig. 7(b)] and MR [diamonds, right, Fig. 7(b)] both peak around  $x = 0.2$ . For higher  $x$ , both  $T_C$  and  $\theta_W$  increase rapidly and nearly triple up to  $x = 0.7$ , while  $H_s$  and MR plateau near their  $x = 0.4$  values. By comparison, in  $2H\text{-Fe}_x\text{TaS}_2$ ,  $T_C$  and  $\theta_W$  peak near  $x = 1/4$  while  $H_s$  and MR peak between the two nominal superstructure concentrations  $x = 1/4$  and  $1/3$  (Fig. 7 of [27]). The proposed theory for  $\text{Fe}_x\text{TaS}_2$  suggests that its behavior is due to the formation of superstructures with MR increasing away from the nominal superstructure compositions due to defects [26]. In  $1T\text{-Fe}_x\text{TiS}_2$  the MR is low near  $x = 1/3$ , and it increases to a peak value as  $x$  decreases to  $x \approx 0.2$ , i.e., upon introducing vacancies in the superstructure. However, the absence of a  $2 \times 2$  superstructure places the peak between the superstructure and the low  $x$  compositions, where sharp switching is not observed, i.e., hysteresis curves do not saturate [up to  $H = 7$  T for  $x \approx 0.1$ , Fig. 7(a)]. In Figs. 7(c) and 7(d), the relationship between MR values and the switching field  $H_s$  in  $1T\text{-Fe}_x\text{TiS}_2$  [orange, panel (c)] is contrasted with that in  $2H\text{-Fe}_x\text{TaS}_2$  [blue, panel (d)]. In both compounds, large

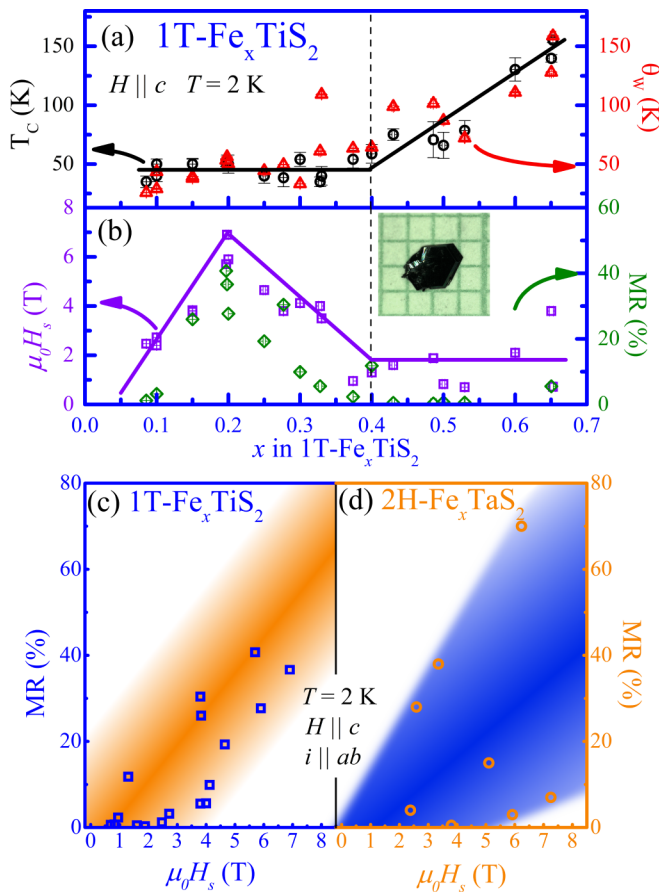


FIG. 7. (a) Phase diagram showing  $T_C$  (top, left axis, down triangle),  $\theta_w$  (top, right axis, up triangle),  $H_s$  (bottom, left axis, square), and MR (bottom, right axis, circle) as a function of  $x$ . (b) MR as a function of switching field  $H_s$  for  $\text{Fe}_x\text{TiS}_2$ . (c) MR as a function of  $H_s$  for  $\text{Fe}_x\text{TaS}_2$  [27].

MR values are correlated to large  $H_s$  values, with a stronger correlation for the Ti system, most likely a reflection of where these compounds are situated in the  $J_3$ - $J_2$  theoretical phase diagram (Fig. 6).

With the discovery of large MR in  $\text{Fe}_x\text{TS}_2$  ( $T = \text{Ti, Ta}$ ), the understanding of the similarities and differences between the two systems brings to light the unanswered questions about magnetically intercalated TMDCs: (i) Why do these two systems show FM order along the  $c$  axis while most others do not? (ii) What singles out  $\text{Fe}_x\text{TS}_2$  ( $T = \text{Ti, Ta}$ ) from other Fe-intercalated TMDCs? (iii) Why do we not see the  $2 \times 2$  superstructure in  $1T\text{-Fe}_x\text{TiS}_2$ ? (iv) Why does glassy behavior appear in  $1T\text{-Fe}_x\text{TiS}_2$  and antiferromagnetic behavior in  $2H\text{-Fe}_x\text{TaS}_2$  for certain  $x$  regimes?

We partially answered question (i) by showing that the easy  $c$  axis for Fe is explained by crystal-field theory, although we have not explained why  $1T\text{-TiS}_2$  and  $2H\text{-TaS}_2$  are the only Fe intercalated TMDCs which show FM behavior. Our model calculation of the coupling constants helps shed light on questions (iii) and (iv). The differences in superstructure and the spin glass behavior are potentially due to the differences in the length scale between the two compounds. However, question (ii) remains unanswered. Many of the other

Fe intercalated TMDCs show AFM behavior [17,21,23,47] precluding them from sharp switching or large MRs. Details explaining this might be elucidated by a more detailed model of the interactions, or an understanding of the nonequilibrium states that form due to the growth dynamics.

Understanding of the physics of low-dimensional systems is of importance due to the plethora of strongly correlated physics that exists from superconductivity to charge-density waves to topology. In particular, the understanding and design of large MR systems is of interest not only because of their rarity, but also because of their technical applications in hard drive technology.

## ACKNOWLEDGMENTS

J.C. and E.M. acknowledge support from DMREF 1629374. C.L.H. is acknowledging partial support from the Gordon and Betty Moore EPiQS Grant No. GBMF 4417. K.L. and N.T. acknowledge support from the National Science Foundation Grant No. DMR-1629382.

## APPENDIX A: SUPPLEMENTARY DATA

The temperature-dependent resistivity in Fig. 8 shows that  $1T\text{-Fe}_x\text{TiS}_2$  is indeed metallic, albeit with weak temperature dependent  $\rho(T)$  above  $T_C$ . The inset shows the determination of the Curie temperature from  $\rho(T)$  (right axis) and  $M(T)$  (left axis) derivatives. Table II summarizes the composition  $x$  dependence of various magnetization and MR parameters for the  $1T\text{-Fe}_x\text{TiS}_2$  series.

## APPENDIX B: SPIN GLASS BEHAVIOR IN $1T\text{-TiS}_2$ FOR $x = 0.1-0.7$

Figure 9 illustrates the frequency dependence of the ac susceptibility for  $x = 0.2$ . The glassy behavior is often characterized by frequency dependence given by Eq. (B1) [48]:

$$f = f_0 \left( \frac{T_f(f)}{T_f(0)} - 1 \right)^{z\nu} \quad (\text{B1})$$

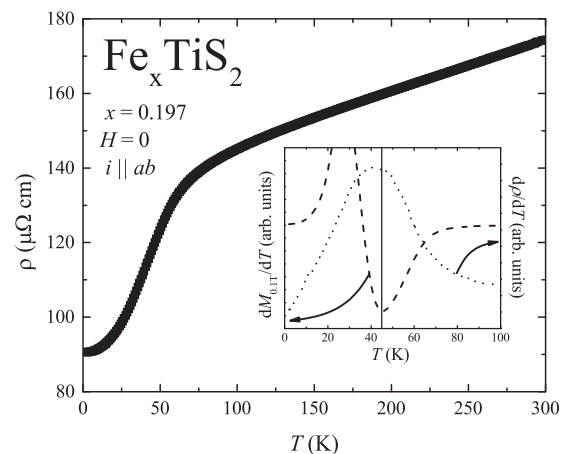


FIG. 8. Temperature-dependent resistivity for  $\text{Fe}_{0.197}\text{TiS}_2$  with  $H = 0$  and  $i \parallel ab$ . Inset:  $d\rho/dT$  (dots) and  $dM/dT$  (dashes) showing determination of Curie temperature.

TABLE II. List of critical temperature and magnetic parameters: Curie Temperature  $T_C$ , Weiss temperature  $\theta_W$ , effective moment  $\mu_{\text{eff}}$ , switching field  $H_s$ , saturated moment  $\mu_{\text{sat}}$ , and magnetoresistance MR as a function of composition  $x$ . An asterisk denotes values for the coercive field and  $M$  (7 T) when no switching field or magnetization saturation was observed up to 7 T.

$\text{Fe}_x\text{TiS}_2$	$T_C$ (K)	$\theta_W$ (K)	$\mu_{\text{eff}}^{\text{ave}}(\mu_B)$	$H_s(2\text{ K})$ (T)	$\mu_{\text{sat}}(2\text{ K}, 7\text{ T})(\mu_{\text{B/f.u.}})$	MR(2 K) (%)
$x = 0.086$	$35.0 \pm 5$	$25.8 \pm 0.1$	3.4	2.5 <sup>a</sup>	1.23 <sup>a</sup>	1.2
$x = 0.1$	$40.0 \pm 5$	$43.5 \pm 0.3$	3.6	7 <sup>a</sup>	1.04 <sup>a</sup>	3.2
$x = 0.15$	$50.0 \pm 4$	$37.8 \pm 0.2$	4.0	3.8	2.39	26
$x = 0.197$	$51.3 \pm 3$	$53.3 \pm 0.1$	3.5	5.8	3.27	40.7
$x = 0.198$	$52.6 \pm 5$	$56.2 \pm 0.2$	3.1	6.9	2.08	36.6
$x = 0.2$	$50.0 \pm 8$	$50.2 \pm 0.1$	3.7	5.9	2.31	27.7
$x = 0.25$	$40.0 \pm 6$	$44.5 \pm 0.3$	3.8	5	2.47	19.3
$x = 0.277$	$38.5 \pm 8$	$49.5 \pm 0.2$	3.6	4.6	2.36	30.4
$x = 0.3$	$54.0 \pm 6$	$33.3 \pm 0.1$	2.2	4.8	2.41	9.9
$x = 0.328$	$35.0 \pm 4$	$60.9 \pm 0.3$	2.5	3.8	1.65	5.6
$x = 0.374$	$54.2 \pm 7$	$63.4 \pm 0.3$	3.0	1.1	1.76	2.3
$x = 0.4$	$58.7 \pm 8$	$64.3 \pm 0.6$	3.0	1.3	4.16	11.8
$x = 0.486$	$70.8 \pm 15$	$101.5 \pm 0.1$	3.0	2	2.82	0.3
$x = 0.5$	$65.9 \pm 11$	$87.0 \pm 0.2$	3.6	0.9	3.98	0.7
$x = 0.5$	$75.1 \pm 5$	$98.8 \pm 0.5$	2.7	2	2.04	0.5
$x = 0.530$	$78.6 \pm 8$	$72.2 \pm 1.6$	2.3	0.8	0.63	0.6
$x = 0.651$	$139.7 \pm 3$	$127.9 \pm 0.7$	3.6	3.8	1.90	4.8

<sup>a</sup>Values are for coercive field and  $M(7\text{ T})$  when no switching field or magnetization saturation was observed up to 7 T.

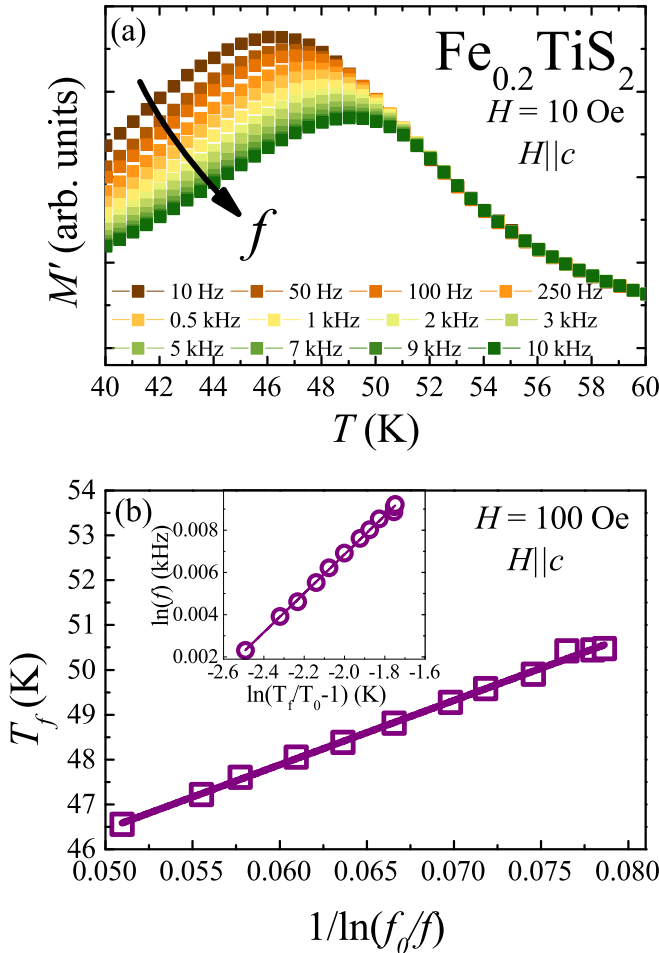


FIG. 9. (a) ac susceptibility showing the frequency dependence of the real component of the moment. (b) Example fits to Eq. (B2) (inset) and to Eq. (B3) (main panel).

or alternatively

$$\ln(f) = f_0 + z\nu \times \ln\left(\frac{T_f(f)}{T_f(0)} - 1\right), \quad (\text{B2})$$

where  $T_f$  is the freezing temperature below which the system is in a spin glass state, defined as the temperature of the peak in susceptibility,  $f_0 = 1/\tau_0$  is a characteristic relaxation frequency with characteristic relaxation time  $\tau_0$ ,  $z$  is the dynamic exponent, and  $\nu$  is the critical exponent. The exponent  $z\nu$  is used as a general indicator for glassiness with typical values for systems with glassy behavior ranging from  $2 \leq z\nu \leq 14$  [49]. In  $1\text{T-Fe}_x\text{TiS}_2$ , spin glass behavior is observed for  $x = 0.1-0.7$ , with  $z\nu$  ranging from 7.61 to 17.21, as seen in Table III.

Further differentiation between spin and cluster glass behavior can be made from Vogel-Fulcher fits to Eq. (B3),

$$T_f(f) = \frac{E_a}{k_B} \frac{1}{\ln(f_0/f)} + T_0, \quad (\text{B3})$$

where  $E_a$  is the activation energy for the spins to overcome the clusters to align with the field,  $k_B$  is the Boltzmann constant, and  $T_0$  is the Vogel-Fulcher temperature, which is a measure of

TABLE III. Values relevant to glass behavior for various compositions  $x$ .

$x$	$T_f(f=0)$ (K)	$z\nu$	$T_0$ (K)
0.1	$20.42 \pm 2$	$10.71 \pm 0.16$	20
0.2	$44.90 \pm 14$	$9.20 \pm 0.12$	43
0.3	$52.35 \pm 2$	$7.61 \pm 0.10$	51
0.530	$71.02 \pm 5$	$14.87 \pm 0.13$	70
0.703	$70.03 \pm 5$	$17.21 \pm 0.18$	67



the interaction strength between clusters [48]. Negative values of  $T_0$  indicated a spin glass system, while the positive values of  $T_0$  are signs of clusters formation [50]. Figure 9(b) illustrates the Vogel-Fulcher fits for  $x = 0.2$ . The  $T_0$  values are positive for all glassy samples with  $x = 0.1-0.703$ , pointing to cluster glass behavior.

### APPENDIX C: ANNEALING STUDY

Choi *et al.* suggested that growth parameters could have an effect on the switching field in  $\text{Fe}_x\text{TaS}_2$ . Specifically, increasing the rate of quenching associated with smaller domains resulted in a greater  $H_s$  attributed to pinning of magnetic domain walls [38]. For comparison, we performed a study to measure the switching field as a function of annealing time (Fig. 10). A sample of  $1\text{T-Fe}_x\text{TiS}_2$  ( $x = 0.198$ ) was annealed in 24 h increments with magnetization ( $H \parallel c$ ,  $T = 2$  K) measured at each annealing step. Before the sample disintegrated at  $t = 5$  days, it showed  $H_s$  increasing with annealing time. It can be expected that a larger domain requires more energy to flip, and hence one assumption is that domain growth is promoted with increasing annealing times, and correspondingly, larger  $H_s$  are required for the domain flip. These two contradictory results, namely that both quenching and annealing increase  $H_s$ ,

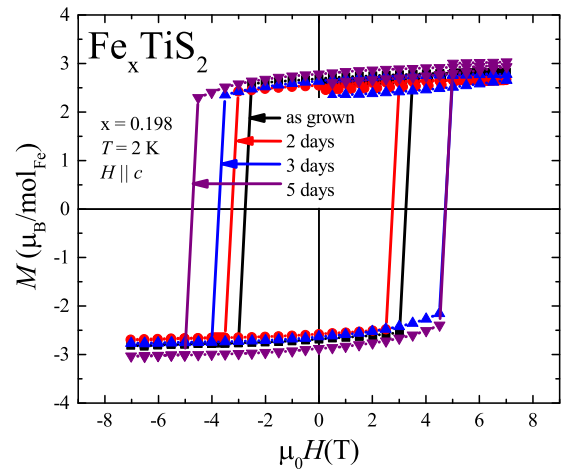


FIG. 10. Magnetization curves for  $\text{Fe}_{0.198}\text{TiS}_2$  showing an increase in switching field as annealing time increases; 48 h increments are shown for clarity.

despite having opposite effects on domain size, in addition to magnetic domain imaging indicating an unusual dendritic formation of domains [51], suggest that domains in this system have an important role to play in magnetic properties.

- [1] Y. Kim, J.-L. Huang, and C. M. Lieber, Characterization of nanometer scale wear and oxidation of transition metal dichalcogenide lubricants by atomic force microscopy, *Appl. Phys. Lett.* **59**, 3404 (1991).
- [2] C.-W. Chen, J. Choe, and E. Morosan, Charge density waves in strongly correlated electron systems, *Rep. Prog. Phys.* **79**, 084505 (2016).
- [3] E. Morosan, H. W. Zandbergen, B. S. Dennis, J. W. G. Bos, Y. Onose, T. Klimczuk, A. P. Ramirez, N. P. Ong, and R. J. Cava, Superconductivity in  $\text{Cu}_x\text{TiSe}_2$ , *Nat. Phys.* **2**, 5440 (2006).
- [4] P. Garoche, J. J. Veysié, P. Manuel, and P. Molinié, Experimental investigation of superconductivity in  $2\text{H-NbSe}_2$  single crystal, *Solid State Commun.* **19**, 455 (1976).
- [5] E. Morosan, K. E. Wagner, L. L. Zhao, Y. Hor, A. J. Williams, J. Tao, Y. Zhu, and R. J. Cava, Multiple electronic transitions and superconductivity in  $\text{Pd}_x\text{TiSe}_2$ , *Phys. Rev. B* **81**, 094524 (2010).
- [6] S. Nagata, T. Aochi, T. Abe, S. Ebisu, T. Hagino, Y. Seki, and K. Tsutsumi, Superconductivity in the layered compound  $2\text{H-TaS}_2$ , *J. Phys. Chem. Solids* **53**, 1259 (1992).
- [7] K. E. Wagner, E. Morosan, Y. S. Hor, J. Tao, Y. Zhu, T. Sanders, T. M. McQueen, H. W. Zandbergen, A. J. Williams, D. V. West, and R. J. Cava, Tuning the charge density wave and superconductivity in  $\text{Cu}_x\text{TaS}_2$ , *Phys. Rev. B* **78**, 104520 (2008).
- [8] J. A. Wilson, F. J. Di Salvo, and S. Mahajan, Charge-density waves and superlattices in the metallic layered transition metal dichalcogenides, *Adv. Phys.* **24**, 117 (1975).
- [9] E. Morosan, D. Natelson, A. H. Nevidomskyy, and Q. Si, Strongly correlated materials, *Adv. Mater.* **24**, 4896 (2012).
- [10] B. Radisavljevic, A. Radenovic, J. Brivio, V. Giacometti, and A. Kis, Single-layer  $\text{MoS}_2$  transistors, *Nat. Nanotechnol.* **6**, 147 (2011).
- [11] Z. Y. Zhu, Y. C. Cheng, and U. Schwingenschlögl, Giant spin-orbit-induced spin splitting in two-dimensional transition-metal dichalcogenide semiconductors, *Phys. Rev. B* **84**, 153402 (2011).
- [12] M. N. Ali, J. Xiong, S. Flynn, J. Tao, Q. D. Gibson, L. M. Schoop, T. Liang, N. Haldolaarachchige, M. Hirschberger, N. P. Ong, and R. J. Cava, Large, non-saturating magnetoresistance in  $\text{WTe}_2$ , *Nature (London)* **514**, 205 (2014).
- [13] J. A. Wilson and A. D. Yoffe, The transition metal dichalcogenides discussion and interpretation of the observed optical, electrical and structural properties, *Adv. Phys.* **18**, 193 (1969).
- [14] M. Naito and S. Tanaka, Electrical transport properties in  $2\text{H-NbS}_2$ ,  $-\text{NbSe}_2$ ,  $-\text{TaS}_2$  and  $-\text{TaSe}_2$ , *J. Phys. Soc. Jpn.* **51**, 219 (1982).
- [15] M. Bayard and M. J. Sienko, Anomalous electrical and magnetic properties of vanadium diselenide, *J. Solid State Chem.* **19**, 325 (1976).
- [16] J. S. Chen, J. K. Wang, S. V. Carr, S. C. Vogel, O. Gourdon, P. Dai, and E. Morosan, Chemical tuning of electrical transport in  $\text{Ti}_{1-x}\text{Pt}_x\text{Se}_{2-y}$ , *Phys. Rev. B* **91**, 045125 (2015).
- [17] S. S. P. Parkin and R. H. Friend,  $3d$  transition-metal intercalates of the niobium and tantalum dichalcogenides. I. Magnetic properties, *Philos. Mag. B* **41**, 65 (1980).
- [18] M. Inoue, M. Matsumoto, H. Negishi, and H. Sakai, Low field ac magnetic susceptibility measurements of intercalation compounds  $\text{M}_x\text{TiS}_2$  ( $\text{M} = 3d$  transition metals), *J. Magn. Magn. Mater.* **53**, 131 (1985).
- [19] F. Hulliger and E. Pobitschka, On the magnetic behavior of new  $2\text{H-NbS}_2$ -type derivatives, *J. Solid State Chem.* **1**, 117 (1970).
- [20] S. S. P. Parkin and R. H. Friend,  $3d$  transition-metal intercalates of the niobium and tantalum dichalcogenides. II. Transport properties, *Philos. Mag. B* **41**, 95 (1980).

- [21] Y. Tazuke, T. Miyashita, H. Nakano, and R. Sasaki, Magnetic properties of  $M_x\text{TiSe}_2$  ( $M = \text{Mn, Fe, Co}$ ), *Phys. Status Solidi C* **3**, 2787 (2006).
- [22] D. R. Huntley, M. J. Sienko, and K. Hiebl, Magnetic properties of iron-intercalated titanium diselenide, *J. Solid State Chem.* **52**, 233 (1984).
- [23] M. A. Buhannic, P. Colombet, M. Danot, and G. Calvarin, The iron electronic characteristics and the crystal dimensionality of the phases  $\text{Fe}_x\text{TiSe}_2$  ( $x = 0.25, 0.38, 0.50$ ), *J. Solid State Chem.* **69**, 280 (1987).
- [24] H. Narita, H. Ikuta, H. Hinode, T. Uchida, T. Ohtani, and M. Wakihara, Preparation and physical properties of  $\text{Fe}_x\text{TaS}_2$  ( $0.15 \leq x \leq 0.50$ ) compounds, *J. Solid State Chem.* **108**, 148 (1994).
- [25] E. Morosan, H. W. Zandbergen, L. Li, M. Lee, J. G. Checkelsky, M. Heinrich, T. Siegrist, N. P. Ong, and R. J. Cava, Sharp switching of the magnetization in  $\text{Fe}_{1/4}\text{TaS}_2$ , *Phys. Rev. B* **75**, 104401 (2007).
- [26] W. J. Hardy, C.-W. Chen, A. Marcinkova, H. Ji, J. Sinova, D. Natelson, and E. Morosan, Very large magnetoresistance in  $\text{Fe}_{0.28}\text{TaS}_2$  single crystals, *Phys. Rev. B* **91**, 054426 (2015).
- [27] C.-W. Chen, S. Chikara, V. S. Zapf, and E. Morosan, Correlations of crystallographic defects and anisotropy with magnetotransport properties in  $\text{Fe}_x\text{TaS}_2$  single crystals ( $0.23 \leq x \leq 0.35$ ), *Phys. Rev. B* **94**, 054406 (2016).
- [28] M. Inoue, K. Sadahiro, and H. Negeshi, Transport studies on relaxation behavior in spin-glass phase of itinerant magnetic intercalate  $\text{Fe}_x\text{TiS}_2$ , *J. Magn. Magn. Mater.* **98**, 60 (1991).
- [29] M. Koyano, M. Suezawa, H. Watanabe, and M. Inoue, Low-field magnetization and AC magnetic susceptibility of spin- and cluster-glasses of itinerant magnet  $\text{Fe}_x\text{TiS}_2$ , *J. Phys. Soc. Jpn.* **63**, 1114 (1994).
- [30] F. Matsukura, Y. Tazuke, and T. Miyadai, ac-susceptibility study of Ising spin glasses:  $\text{Fe}_x\text{TiS}_2$ , *J. Phys. Soc. Jpn.* **58**, 3355 (1989).
- [31] H. Negishi, S. Ōhara, M. Koyano, M. Inoue, T. Sakakibara, and T. Goto, Anisotropic spin-glass and cluster-glass of layered  $\text{Fe}_x\text{TiS}_2$  crystals, *J. Phys. Soc. Jpn.* **57**, 4083 (1988).
- [32] M. Koyano, S. Horisaka, H. Negishi, M. Sasaki, M. Inoue, N. Suzuki, and K. Motizuki, Magnetic scattering of conduction carriers in  $3d$  transition-metal intercalates of  $M_x\text{TiS}_2$  ( $M = \text{Mn, Fe, Co, and Ni}$ ), *J. Low Temp. Phys.* **78**, 141 (1990).
- [33] T. Satoh, Y. Tazuke, T. Miyadai, and K. Hoshi, Ferromagnetic and reentrant spin glass properties in an Ising magnet  $\text{Fe}_x\text{TiS}_2$ , *J. Phys. Soc. Jpn.* **57**, 1743 (1988).
- [34] H. Negishi, A. Shoube, H. Takahashi, Y. Ueda, M. Sasaki, and M. Inoue, Magnetic properties of intercalation compounds  $M_x\text{TiS}_2$  ( $M = 3d$  transition metal), *J. Magn. Magn. Mater.* **67**, 179 (1987).
- [35] T. Yoshioka and Y. Tazuke, Magnetic properties of  $\text{Fe}_x\text{TiS}_2$  system, *J. Phys. Soc. Jpn.* **54**, 2088 (1985).
- [36] J. Dijkstra, P. J. Zijlema, C. F. van Bruggen, C. Haas, and R. A. de Groot, Band-structure calculations of  $\text{Fe}_{1/3}\text{TaS}_2$  and  $\text{Mn}_{1/3}\text{TaS}_2$ , and transport and magnetic properties of  $\text{Fe}_{0.28}\text{TaS}_2$ , *J. Phys.: Condens. Matter* **1**, 6363 (1989).
- [37] K.-T. Ko, K. Kim, S. B. Kim, H.-D. Kim, J.-Y. Kim, B. I. Min, J.-H. Park, F.-H. Chang, H.-J. Lin, A. Tanaka, and S.-W. Cheong, RKKY Ferromagnetism with Ising-Like Spin States in Intercalated  $\text{Fe}_{1/4}\text{TaS}_2$ , *Phys. Rev. Lett.* **107**, 247201 (2011).
- [38] Y. J. Choi, S. B. Kim, T. Asada, S. Park, W. Wu, Y. Horibe, and S.-W. Cheong, Giant magnetic coercivity and ionic superlattice nano-domains in  $\text{Fe}_{0.25}\text{TaS}_2$ , *Europhys. Lett.* **86**, 37012 (2009).
- [39] M. Inoue, H. P. Hughes, and A. D. Yoffe, The electronic and magnetic properties of the  $3d$  transition metal intercalates of  $\text{TiS}_2$ , *Adv. Phys.* **38**, 565 (1989).
- [40] Y. Kuroiwa, M. Nishimura, R. Nakajima, H. Abe, and Y. Noda, Short-range order and long-range order of Fe atoms in a spin-glass phase and a cluster-glass phase of intercalation compounds  $\text{Fe}_x\text{TiS}_2$ , *J. Phys. Soc. Jpn.* **63**, 4278 (1994).
- [41] Y. Kuroiwa, M. Nishimura, Y. Noda, and Y. Morii, Neutron powder diffraction study of intercalation compound  $\text{Fe}_x\text{TiS}_2$ , *Physica B* **213–214**, 396 (1995).
- [42] Y. Kuroiwa, H. Honda, and Y. Noda, Neutron magnetic scattering of intercalation compounds  $\text{Fe}_x\text{TiS}_2$ , *Mol. Cryst. Liq. Cryst. Sci. Technol. Sec. A* **341**, 15 (2000).
- [43] M. A. Ruderman and C. Kittel, Indirect exchange coupling of nuclear magnetic moments by conduction electrons, *Phys. Rev.* **96**, 99 (1954).
- [44] T. Kasuya, A theory of metallic ferro- and antiferromagnetism on Zener's model, *Prog. Theor. Phys.* **16**, 45 (1956).
- [45] K. Yosida, Magnetic properties of Cu-Mn alloys, *Phys. Rev.* **106**, 893 (1957).
- [46] C. M. Fang, R. A. de Groot, and C. Haas, Bulk and surface electronic structure of  $1T - \text{TiS}_2$  and  $1T - \text{TiSe}_2$ , *Phys. Rev. B* **56**, 4455 (1997).
- [47] S. J. Hillenius and R. V. Coleman, Magnetic susceptibility of iron-doped  $2H\text{-NbSe}_2$ , *Phys. Rev. B* **20**, 4569 (1979).
- [48] J. A. Mydosh, *Spin Glasses: An Experimental Introduction* (Taylor and Francis, London, 1993).
- [49] E. Svanidze and E. Morosan, Cluster-glass behavior induced by local moment doping in the itinerant ferromagnet  $\text{Sc}_{3.1}\text{In}$ , *Phys. Rev. B* **88**, 064412 (2013).
- [50] V. K. Anand, D. T. Adroja, and A. D. Hillier, Ferromagnetic cluster spin-glass behavior in  $\text{PrRhSn}_3$ , *Phys. Rev. B* **85**, 014418 (2012).
- [51] M. D. Vannette, S. Yeninas, E. Morosan, R. J. Cava, and R. Prozorov, Local-moment ferromagnetism and unusual magnetic domains in  $\text{Fe}_{1/4}\text{TaS}_2$  crystals, *Phys. Rev. B* **80**, 024421 (2009).